



HAL
open science

Nanomechanical signatures of degradation-free influence of water on halide perovskite mechanics

Isaac Buchine, Irit Rosenhek-Goldian, Naga Prathibha Jasti, Davide R Ceratti, Sujit Kumar, David Cahen, Sidney R Cohen

► **To cite this version:**

Isaac Buchine, Irit Rosenhek-Goldian, Naga Prathibha Jasti, Davide R Ceratti, Sujit Kumar, et al.. Nanomechanical signatures of degradation-free influence of water on halide perovskite mechanics. Communications Materials, 2022, 3 (1), pp.70. 10.1038/s43246-022-00287-7 . hal-03884115

HAL Id: hal-03884115

<https://hal.science/hal-03884115>

Submitted on 5 Dec 2022

HAL is a multi-disciplinary open access archive for the deposit and dissemination of scientific research documents, whether they are published or not. The documents may come from teaching and research institutions in France or abroad, or from public or private research centers.

L'archive ouverte pluridisciplinaire **HAL**, est destinée au dépôt et à la diffusion de documents scientifiques de niveau recherche, publiés ou non, émanant des établissements d'enseignement et de recherche français ou étrangers, des laboratoires publics ou privés.

Nanomechanical signatures of degradation-free influence of water on halide perovskite mechanics

Isaac Buchine ^{1,5}, Irit Rosenhek-Goldian ^{2,5}, Naga Prathibha Jasti ¹, Davide R. Ceratti^{3,4}, Sujit Kumar ^{1,3}, David Cahen ^{1,3}✉ & Sidney R. Cohen ²✉

Humidity is often reported to compromise the stability of lead halide perovskites or of devices based on them. Here we measure the humidity dependence of the elastic modulus and hardness for two series of lead halide perovskite single crystals, varying either by cation or by anion type. The results reveal a dependence on bond length between, hydrogen bonding with, and polarizability/polarization of these ions. The results show an intriguing inverse relation between modulus and hardness, in contrast to their positive correlation for most other materials. This anomaly persists and is strengthened by the effect of humidity. This, and our overall findings are ascribed to the materials' unique atomic-scale structure and properties, viz nano-polar domains and strong dynamic disorder, yet high-quality average order. Our conclusions are based on comparing results obtained from several different nano-indentation techniques, which separate surface from bulk elastic modulus, and probe different manifestations of the hardness.

¹Bar-Ilan University, Dept. of Chemistry and Bar-Ilan Inst. of Nanotechnol. & Adv. Mater., Ramat Gan, Israel. ²Dept. of Chemical Research Support, Weizmann Inst. of Science, Rehovot, Israel. ³Dept. of Mol. Chem. & Materials Science, Weizmann Inst. of Science, Rehovot, Israel. ⁴CNRS, UMR 9006, IPVF, Institut Photovoltaïque d'Île-de-France, 18 Boulevard Thomas Gobert, 91120 Palaiseau, France. ⁵These authors contributed equally: Isaac Buchine, Irit Rosenhek-Goldian. ✉email: David.cahen@weizmann.ac.il; sidney.cohen@weizmann.ac.il

Halide Perovskites (HaPs) with ABX_3 stoichiometry, where A is a monovalent cation, Cs^+ , methylammonium ($MA^+ - CH_3NH_3^+$), or formamidinium ($FA^+ - CH(NH_2)_2^+$), B is a divalent cation, usually Pb^{2+} , and X is a halide mono-anion, (Cl^- , Br^- , or I^-), have remarkable optoelectronic properties. This has led to their promotion for the next-generation semiconductor-based devices^{1,2}. Long carrier lifetimes, reasonable charge carrier mobilities, facile low temperature solution preparation of polycrystalline thin films^{3,4} with low to ultra-low defect densities, high optical absorption coefficients and tunable bandgaps, collectively set the stage for incorporating these materials in the semiconductor industry^{5–10}. Accordingly, they are outstanding candidates for use in a variety of technologies, including photovoltaic solar cells, light-emitting diodes, radiation detectors^{8,11–13}, and flexible^{13–15} and wearable electronics.

These last two applications, combined with the fact that mechanical properties of these materials may influence ion migration dynamics and non-radiative recombination at strain-induced defects, highlight the need to understand their mechanical properties. A number of studies have examined the optoelectronic properties of humidity-degraded HaPs, both experimentally, and through modelling^{16–20}, while recent reviews summarize the current status of the HaP – water interaction^{21,22}. The structural changes accompanying this interaction necessarily influence the mechanical properties, and indeed such relationships have been experimentally and theoretically studied. There is general consensus that the extent of material degradation and mechanical change varies according to the extent of humidity exposure^{19,20,23,24}. Whereas mild exposure to humidity results in reversible monohydrate formation, prolonged exposure was found to promote the formation of the dihydrate, which leads irreversibly to $MAPbI_3$ decomposition into PbI_2 ^{25–27}. The degradation is a complex process, which is also affected by exposure to light, by elevated temperatures, and may occur over long time scales, and even in inert atmospheres²⁸. Studies also indicate that higher concentration of Br in $MAPb(I_{1-x}Br_x)_3$ decreases the tendency for degradation, possibly because the cubic phase is more stable than the tetragonal one²⁹, in addition to the fact that water absorption in $MAPbI_3$ is more energetically favorable than in $MAPbBr_3$ ³⁰.

The detailed mechanism by which H_2O enters the crystal is not yet resolved. While excess water can dissolve the methylammonium ions²⁵, an atomistic computational study of H_2O interaction with $MAPbI_3$ found no evidence for a chemical reaction between H_2O and MA^+ , suggesting that higher H_2O concentration is needed to induce degradation through lattice distortion³¹. An experimental study on thin polycrystalline films by X-ray diffraction (XRD), quartz crystal microbalance, and infrared (IR) spectroscopy verified that there is no interaction between water and MA^+ , if water enters into the lattice under ambient conditions (around 50% relative humidity (RH)). Formation of monohydrate occurred within several minutes at high (>95%) relative humidity. Additionally, water uptake was found to be influenced by sample porosity, i.e., pulverizing a single crystal or measuring on more porous decomposed monohydrate resulted in lower stability against humidity than that of the original single crystal³². Other works found the formation of monohydrate in ambient at long exposure (days) or high humidity (>80%)^{25,33}. An acid–base reaction in which water captures a proton from the MA moiety was also suggested to initiate degradation³⁴. To date there is no direct evidence for the formation of H_3O^+ ; ab initio computational studies found hydronium to be unstable to back-proton transfer to re-form the MA cation in $MAPbI_3$ and $MAPbBr_3$ ³⁵, by deprotonation of methylammonium to methylamine, $H_2O + CH_3NH_3^+ \rightarrow H_3O^+ + CH_3NH_2 \uparrow$. However, it was proposed that the

degradation is induced by interaction with basic hydroxyl radicals, OH^\bullet , formed on surfaces of metal oxides, such as TiO_2 that contact the perovskite (e.g., as selective contact layers in a solar cell). These radicals can deprotonate MA^+ , $OH^\bullet + [CH_3NH_3PbI_3]_n \rightarrow H_2O + (CH_3NH_2)_{n-1}[PbI_3]_n + CH_3NH_2 \uparrow$, in a process similar to that of interaction with H_2O ³⁵.

Two other atomistic, theoretical studies reached contradicting conclusions about the influence of H_2O on the HaP crystalline structure. Mosconi et al. found that methylammonium and iodide-terminated $MAPbI_3$ crystals will hydrate rapidly, degrading the surface by the dissolution of MA^+ and iodide ion into liquid water, whereas a Pb^{2+} and iodide-terminated surface will hydrate but remain intact³⁶. They further found that water in the bulk of the crystal led to only minimal distortion of the lattice. On the contrary, Tong et al. found that high water concentrations in the bulk result in extensive lattice distortion³⁷. Also grazing-angle incidence X-ray diffraction (GIXRD) measurements on $CH_3NH_3PbI_3$ films in humid environment pointed toward hydration as the initial decomposition step. This conclusion was supported by evidence of the formation of a hydrated intermediate, containing isolated $(PbI_6)_4^-$ octahedra²⁴.

Because the HaPs typically are prepared either as thin films or crystals of mm dimensions, the study of their mechanical properties has typically been performed using nanoindentation and/or atomic force microscopy-based techniques. Mamun and coworkers investigated films of $MAPbI_{3-x}Cl_x$ by instrumented nanoindentation under long-time (several days) exposure to ambient conditions³⁸. They found an initial rise in modulus (E) and hardness (H), followed by a decrease in their values and eventually another increase at even longer times (we parenthetically note that throughout this manuscript we refer to hardness and elastic modulus, whereas technically the measured values are indentation modulus and indentation hardness. The latter terms refer to the fact that the uniaxial measurement performed by atomic force microscopy (AFM) or nanoindentation averages over the elastic properties in the different directions, which returns somewhat different values than the Young's modulus for an anisotropic material, see ref. 39). These changes were related to chemical and structural changes on the surface as indicated by corresponding changes in crystal size. Spina and coworkers measured mechanical properties using nanoindentation⁴⁰. They investigated the effect of exposing $MAPbI_3$ single crystals to ambient 30–50% relative humidity, also over long times (months). They found that E and H dropped monotonically to about 20% of their initial values, which, though, could be largely regenerated by dipping the sample in methylammonium iodide solution. Liao and coworkers measured the elastic modulus of both films and single crystals of $MAPbI_3$ by AFM, an approach that is sensitive to the outer few nm of the surface³³. The measurements were carried out for several days in a controlled atmosphere of 50% relative humidity. A pseudo-oscillatory behavior was observed with E first rising, then falling then rising and falling again. Together with XRD and morphological analysis, they proposed the formation of $MAPbI_3$ monohydrate with PbI_2 forming on the surface within several days. Differences in experimental conditions and crystalline form (film vs. single crystal, different orientation of the exposed faces) of the HaP in the above-mentioned studies, make it hard to draw specific conclusions about the effect of humidity on the HaP mechanics.

Although as summarized above, previous computational and experimental work studied the effects of water on the crystal structure and changes occurring during long-term exposure to humidity, the differences between the various experimental conditions, including the form of the material (single or polycrystalline), do not enable drawing general conclusions with



Fig. 1 Pb-based HaP single crystals used in this study. Horizontally: MAPbX_3 ($X = \text{Cl}, \text{Br}, \text{and I}$); vertically: APbBr_3 ($A = \text{Cs}, \text{MA}, \text{and FA}$).

atomic-level insights. To address this question, we use single crystals of HaPs to study the effect of humidity on their nanomechanical properties. We use HaP single crystals rather than polycrystalline films to minimize the contribution from grain boundaries and interfaces that might affect reproducibility and in fact alter the overall response to water exposure. For instance, the large concentration of uncoordinated bonds in small ($< \mu\text{m}$) grained polycrystalline films are amenable to the formation of hydrogen bonds and the eventual development of a molecular water layer²². To understand the role of HaP composition, we prepared and studied two sets of Pb-based HaP single crystals (see Fig. 1): in one, the methylammonium (MA)-lead set, the halide was varied ($\text{MAPb-Cl}_3, \text{-Br}_3, \text{-I}_3$) and in the other, the lead-bromide set, the A-site cation was varied ($\text{Cs-}, \text{MA-}, \text{FA-PbBr}_3$). The former set is of interest because changing the halide (X) in HaPs is known to influence the opto-electronic^{41,42} and mechanical properties^{43,44}. Additionally, reversibility of the changes was studied since humidity has been reported to induce material degradation as well as mechanical changes, both of which depend on the extent of humidity exposure^{19,20,23,24}. We find that the response to humidity depends on the HaP composition.

A key to our approach is to measure the elastic moduli and hardness values by two different approaches – instrumented nano-indentation (NI) and atomic force microscopy (AFM), in addition to some other independent physical measurements. Although both AFM and NI can be used to measure E and H of materials, they differ in the physical principles by which the force is applied and how the material's response to the force is quantified. Comparison of elastic modulus values measured by two different techniques, NI to monitor the crystal bulk properties and contact resonance - atomic force microscopy (CR-AFM) to monitor the outer surface properties, shows how differences in both the surface sensitivity and fundamental data used to quantify each property give insights into the micro- and nano-scale mechanical processes.

Searching for a correlation between trends of modulus change with humidity and a physicochemical characteristic, we find that these trends can be explained by the polarizability of the X-site anion (by the cations) and the polarization (or polarizing) power of the A-site cation (on the halide anions) for near-surface measurements (CR-AFM), but not for the bulk (NI) ones. This can be related to structural differences between surface and bulk sites. In contrast to the influence of humidity on other material classes, here higher humidity leads to increased modulus, an

anomaly, which can be rationalized using the arguments provided below. Hardness, however, follows the well-known trend of hydration-correlated softening. Thus, E and H are anti-correlated, which adds to the anomaly. The NI results reveal the interesting trade-off between elastic (reversible) and plastic (irreversible) deformation of the crystals under applied load, while AFM-based traditional hardness measurements reveal differences in the extent of plastic deformation between the studied materials and point to the role of water as a plasticizer.

Results and Discussion

Preliminary characterizations. The crystals were characterized by XRD, Raman spectroscopy, and photoluminescence. Humidity-dependent XRD measurements showed no change in $\theta - 2\theta$ or rocking curve measurements on a MAPbBr_3 crystal (Supplementary Figure 1). Similarly, Raman spectroscopy did not show changes in the FA-related vibrational modes of FAPbBr_3 (Supplementary Figure 2). There was no phase change with humidity, as also seen from the constancy of the photoluminescence emission spectra of MAPbBr_3 and CsPbBr_3 crystals; for FAPbBr_3 two different crystal batches showed a small frequency shift (Supplementary Figures 3 and 4). This is likely due to the high temperature, rapid crystal growth these crystals required (see experimental section). The observation that after a “Low \rightarrow High \rightarrow Low” humidity exposure cycle the spectra become narrower for FAPbBr_3 and to some extent also for the other two bromide perovskites (Supplementary Figure 4) is likely related to some annealing occurring in the humid ambient. Related results have been reported previously for polycrystalline lead halide perovskite films and single crystals^{45–48}. Together, these measurements indicate that the humidity exposure led to only minor inclusion of water in the crystal. Nonetheless, significant changes in the mechanical properties took place.

Rationale for nanomechanical measurement methodology.

Nanomechanical properties, notably hardness and elastic modulus are conveniently measured using instrumented nano-indentation coupled with Oliver & Pharr analysis (O & P)⁴⁹. In some cases, atomic force microscopy is more appropriate, or can provide complementary information⁵⁰. It should be stressed here that the fundamental assumptions implicit in the O & P approach (e.g., isotropic, homogeneous sample) are not always met (for instance HaPs can exhibit large mechanical anisotropy⁵¹). Nonetheless the techniques are valid for approximate or comparative studies, and this methodology has been adopted as an international standard⁵². Here, the comparative approach, as well as combining and contrasting results from NI and AFM is a central part of our study. Furthermore, in the present study, the regime of moderate humidity exposure has been adapted to enhance the reversibility of the exposure to water. Both NI and AFM were performed at comparable environments, so that similarities and differences in the observed trends in these techniques can be compared to give additional insight into the nano-scale processes.

Elastic modulus. The results for the elastic modulus, E , from using continuous stiffness measurement and averaged over deformation depths of 300–800 nm in the nano-indenter (Fig. 2a), are within the range of values reported for HaP elastic moduli in the literature^{43,44,53,54}. We use these relatively large depths to avoid artifacts due to surface roughness and irregularities in the tip shape, as recommended in the literature⁵⁵. The elastic modulus of all crystals increases with humidity (except CsPbBr_3 , which shows small changes at the level of

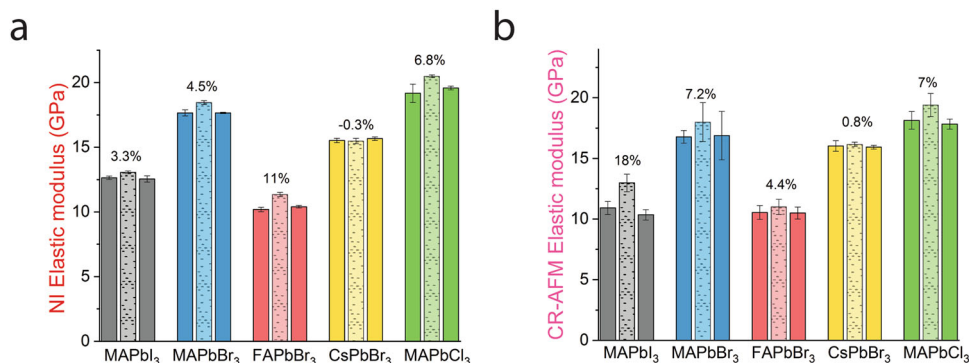


Fig. 2 Elastic modulus results. In each triplet the solid bars represent measurements performed in the dry state ($RH \leq 10\%$), left for before and right for after measurements represented by the dotted (middle) bars which were performed in the humid state ($RH 55\text{--}60\%$). The percentage values represent difference between dry and humid states for each set. **a** Data obtained from NI measurements over 300–800 nm depth; **b** Near-surface elastic moduli, measured at <10 nm depth by CR-AFM. Error bars represent standard deviation of the measurements.

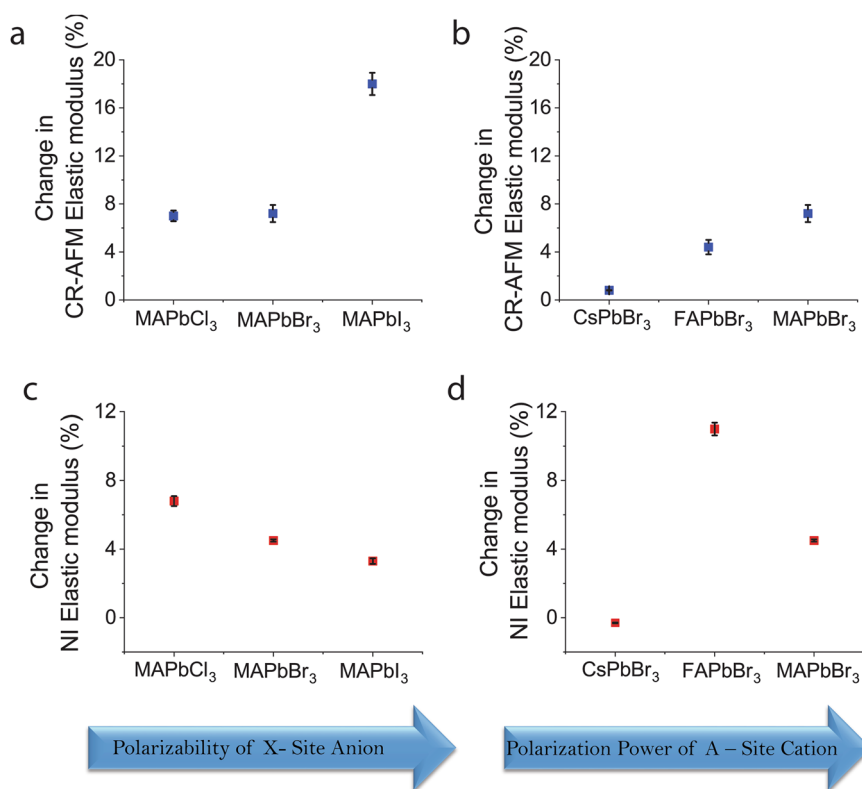


Fig. 3 Influence of ion polarization power/polarizability on modulus. Percentage change in E from CR-AFM (contact resonance) (**a**, **b**) and NI (nano-indenter) (**c**, **d**) between dry and humidity-exposed crystals, as function of X-site anion polarizability (**a**), (**c**), and as function of polarity of A-site cation (**b**), (**d**). Error bars are computed from the relative error of the quotient, using standard deviation of individual values.

experimental uncertainty), consistent with bond stiffening in the presence of water.

In contrast to the NI measurements, which are recorded at depths of hundreds of nm, AFM can measure modulus values for the outer few nm (see experimental section). Comparing the results of the two approaches thus can help elucidate the extent of water penetration into the crystal. The AFM-based measurements were performed using the contact resonance (CR-AFM) method (Fig. 2b). CR-AFM is sensitive to surface depths on the order of the contact radius, which was about 20 nm. For a given crystal, at the surface, E is higher for the humid than the dry state, as is the case with NI measurements. However, cross-comparison between the crystals shows some interesting differences. Specifically, Fig. 3 compares the trends in modulus change at different humidity

conditions vs. the relevant anion polarizabilities and cation polarization power.

The changes between dry and humid conditions in the CR-AFM - derived modulus values, become larger with increasing polarizability of the X-site anion (although the change between Cl and Br is negligible), but the NI-derived ones monotonically decrease. For the A-site cation series, the changes for moduli, derived from CR-AFM, increase monotonically with increase in cation polarization power, whereas for the NI-derived values there is no clear trend (Fig. 3). These results establish a clear difference between the influence of ion polarization power/polarizability on/near the surface, relative to the bulk. Effects of surface polarity are known to influence water adsorption onto hybrid perovskite surfaces³¹. Ab initio Density Functional Theory

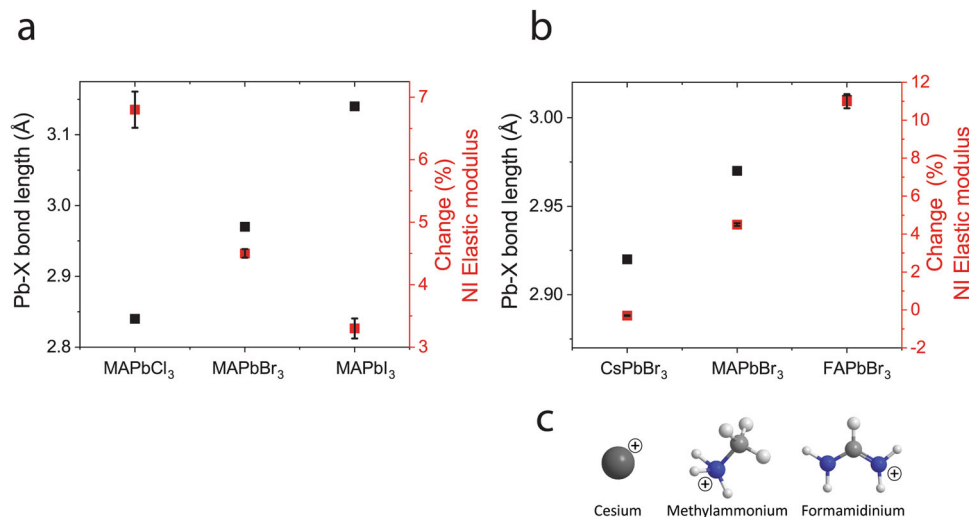


Fig. 4 Humidity dependence of of NI elastic modulus on Pb-X bond length and H-bonding. Pb-X bond length (black) and % change in NI elastic modulus between dry and humid states (red) (a) plotted for the series of X anions and (b) for the series with different A cations. Error bars are computed from the relative error of the quotient, using standard deviation of individual values. (c) scheme showing potential for H-bonding for the different cations, in terms of H atoms (white spheres), available to participate in the bonding; dark grey sphere: Cs; blue sphere: N; light grey sphere: C.

(DFT) calculations confirm that water is more strongly adsorbed on MAPbI₃ than on MAPbBr₃, FAPbI₃ and CsPbI₃^{30,35}. The CR-AFM results show that this adsorption serves to enhance the increase in the elastic modulus of the MAPbI₃ crystal surface at high humidity more than for the other HaPs (Fig. 2b), supporting the predicted stronger water interaction with MAPbI₃ compared to the other HaPs as found from computations as noted above. That this interaction is much stronger (6 times for MAPbI₃, by far the largest difference between the two methods, among all HaPs studied here) at the surface than in the bulk can be due to the enhanced ability for structural deformation at and near the surface. As recently suggested by Chen et al., a hydrated perovskite surface layer on the MAPbI₃ may prevent vapor penetration into the bulk of the crystal²². Exposure of MAPbI₃ films to high humidity resulted in defect-free highly oriented crystals with significantly fewer grain boundaries and electronic defects than in the dry films^{45,46}. Related results have been reported previously for polycrystalline lead halide perovskite films⁴⁷, and the effect was recently studied by us for single crystals of MAPbI₃⁴⁸.

For our single crystal samples, we cannot rule out humidity-induced surface annealing, but this cannot be definitively shown. No surface structural changes on the surface are detectable in our AFM scans. This contrasts the findings for larger and longer humidity exposures where clear surface structural differences were observed^{33,38,40}. We have calculated the diffusion of water into these materials using proton diffusion coefficients, finding that it may reach depths of 3–4 μm. This depth represents the bulk for the purpose of the studies we report on here. This also fits the estimated depth of H₂O in-diffusion into MAPbI₃ under similar humidity conditions^{56–58}, as well as our recent TGA-MS and GI-XRD experiments⁵⁹. A depth profile of H₂O could follow a gradient of [H₂O] decreasing with increasing depth from the surface. This is not evident in the depth profiles of E and H (Supplementary Figure 5) but only a sharp gradient would be expected to influence the shape of such curves because the volume probed by the indenter tip is significantly larger than that within the contact area. A gradient very near the surface is not discernable in the nanoindenter measurements: surface effects prevent reliable measurement of E and H in the nanoindenter at the outer surface (under 100 nm). Strain is likely stronger near the

surface, decreasing with depth and is relevant for the depths probed here (from a few nm up to a few μm). In any scenario, the presence of water together with energetic and (possibly microscopic) structural differences at the crystal (near) surface can lead to a difference between surface and bulk behavior.

The results shown in Fig. 3 establish the effect of ion polarization power/polarizability on the strength of the surface-water interactions. For the NI experiments (Fig. 3c, d), which reflect properties for depths of hundreds of nm, the modulus change with humidity cannot directly depend on the adsorption of water at the surface; instead, these results should relate to some direct or indirect effect of water on the bulk material.

The plot in Fig. 4a traces the dependence of % change of the NI modulus with RH and of Pb-X bond length, on the X anion in MAPbX₃ and in Fig. 4b on the A cation in APbBr₃. For the series of different X-site anions, the extent of change of the NI modulus decreases with increasing bond length. Thus, in this series, the longer the bond the less effect water has on the bond stiffness in the bulk.

When the same data types are plotted for the A site cation APbBr₃ series, the trend is reversed (Fig. 4b). This can be explained by the combined influence of lattice distortion and electrostatic interactions: although the Pb-X framework largely determines the mechanical behavior, short-range Coulombic interactions between the A cation and PbI₆ cage are also important⁶⁰. In the cation series, the MA ion is smaller than the FA one and, so it was argued, strains the Pb-X framework less⁶¹. As mentioned in the introduction, strong water-MA interactions are not found under the humidity conditions probed here. Nonetheless, the water still fills the lattice leading to significant strain^{31,32}. Furthermore, the different distribution and number of potential H-bonds results in stronger computed overall H-bond energy between organic cation and halide for FA than for MA in APbBr₃, and thus inhibited rotation for the former relative to latter⁶².

The trend in NI elastic modulus for the 3 cations can be explained by the extent of their interaction with water, which is smallest for Cs, larger for MA and greatest for FA (see Fig. 4c for the three cations and their potential for interaction with H₂O via H-bonding). Cs is only weakly hydrated^{63,64}, while MA and FA have stronger interaction through their amine group(s). These

groups can form both internal hydrogen bonds between the ammonium entity and the halide, as well as external hydrogen bonds with trapped water. In particular, FA can form both types of hydrogen bonds simultaneously, while MA can form only one type or the other, set by their number of H-bonding sites available. The trend of intra-crystalline H-bonding is a topic that is not completely resolved: computations and some experiments indicate that the internal H-bond between amine and halide is weaker for FA than for MA^{53,65} and that this is also the trend for bonding to water³⁰. However, other computational work found that the internal H-bonding energy is higher for FA- than for MA in APbBr₃⁶².

The presence of water can compete with the internal bonding and alter the electrostatic interactions²⁶ which influence the mechanical properties. This interpretation fits with the findings of Sun et al. regarding the major influence of H bonding on the elastic modulus of halide perovskites⁶⁵. Stronger H-bonding promotes the tendency for water to fill the cavity and stiffen the structure, but as the framework's size increases, this effect decreases, due both to steric factors and to shielding of the short-range Coulomb attraction.

Hardness. Whereas the elastic modulus is directly related to bond stiffness, an intrinsic material property, hardness is less a fundamental and more an engineering property, which can be thought of as the ease with which a material undergoes plastic deformation. This can be related to yield strength (the stress level resulting in plastic deformation), and work hardening exponent (which governs relationship between stress and strain)⁶⁶. Interestingly hardness is often inversely correlated with fracture toughness (resistance to crack formation). Furthermore, hardness does not always correlate with mechanical robustness, whereas the ratio between H and E (*vide infra*) is an important indicator of resistance to plastic deformation^{66,67}.

In a classical indentation experiment, the hardness is directly related to the size of the imprint left by pressing the indenter into the surface at a fixed load. In nano-indentation (NI) this size is not directly measured, but estimated from the maximum indentation depth and known tip shape. This estimation, employed in the Oliver and Pharr analysis⁴⁹, includes a component of the elastic deformation. The correction for this component is, for some material types, incomplete as it presumes that radial deformation is negligible³⁹. In addition, this analysis does not account for pile-up of material at the perimeter of the indentation imprint. Thus, analyzing the results of nano-indentation experiments provides only partial information. This is discussed below for the case when NI hardness measurements under dry and wet conditions yield similar values, but imprint sizes, observed in AFM topography, and even optical images in the nano-indenter show much larger imprints under humid conditions.

NI results in Fig. 5a show that there is an inverse relation between hardness and humidity. Hardness measured in the NI (which will be referred to as NI hardness) generally decreases as the atmosphere is more humid; for MAPbCl₃, MAPbBr₃, CsPbBr₃ hardness decreases by 31%, 34%, and 12%, respectively at high humidity and recovers after return to the low humidity conditions. MAPbI₃ and FAPbBr₃, though, do not show this behavior, but rather an insignificant change with humidity. While no detectable changes in NI hardness are found for these two crystals, the sizes of the indentations differ significantly, as can be seen in the optical microscope image (Supplementary Figure 6).

This effect is also observed on AFM images scanned after the CR-AFM measurements (Supplementary Figure 7), which are done at loading forces 2 orders of magnitude below those used in

the nano-indenter. At low humidity, no residual imprints are observed in the measured region, as is typically seen in such measurements. However, when RH was raised to 75% (higher than the RH used for the other results reported here) significant plastic deformation was observed even under these low loads, as can be seen by comparing Supplementary Figure 7d with Supplementary Figure 7i.

To understand the changes in the plastic vs. elastic deformation components we analyze another quantity, namely the change in the h_f / h_{max} ratio with different relative humidity conditions. As seen in Fig. 5c, h_{max} and h_f are the penetration depth under maximum load and the residual depth remaining after the release of the force on the indenter. These are experimental quantities obtained directly from the force curve. For a purely plastic indentation, their ratio will be 1. Smaller ratios indicate the increasing contribution of elastic processes with a limiting value of zero for purely elastic behavior. Of all the crystals examined, FAPbBr₃ has the most atypical results (Fig. 5c). First of all, h_f / h_{max} is much lower than for all the other crystals in the dry state. MAPbI₃ also has a relatively small ratio of h_f / h_{max} , lying between that of FAPbBr₃ and the other HaPs. After exposure to humidity, h_f / h_{max} for FAPbBr₃ rises to values comparable to that of the other crystals. Upon drying, the ratio again drops. The change in MAPbI₃ is less dramatic – the change in h_f / h_{max} between the dry and humid states for FAPbBr₃ is about 10x that obtained for the other crystals, while for MAPbI₃ h_f / h_{max} it is about two times larger than that of the others (apart from FAPbBr₃). Since neither FAPbBr₃ nor MAPbI₃ undergo any significant change in NI hardness with humidity (Fig. 5a), the data of Fig. 5a, c, taken together indicate that the increase in the plastic part of the deformation with humidity (Fig. 5c) is countered by a decrease in the elastic deformation, because higher modulus means smaller deformation. Notably, referring to Fig. 2a, the change in E with humidity was largest for FAPbBr₃ amongst all the crystals studied, while the change was largest for MAPbI₃ for CR-AFM measurements.

These comparisons are extremely important to understand the processes occurring during elastic-plastic deformation. As noted above, the classic relations used to derive H and E from nano-indenter load vs. deformation curves⁴⁹ assume elastic-plastic loading and elastic unloading. Deviations from the assumed behavior can occur under certain conditions, depending on the overall ratio of elastic to plastic work, gauged by the relative values of H and E . For materials with $H/E < 0.1$, as is the case for the materials studied here, it has been shown that h_f / h_{max} is linearly related to H/E ⁶⁸. With some simplifying assumptions, it can also be shown that this ratio equals the ratio of plastic to total work performed during the indentation cycle⁶⁹. Bolshakov and Pharr have discussed the use of h_f / h_{max} to determine the material properties when the H/E ratio is large⁷⁰. Specifically, they show that the value of h_f / h_{max} is an indicator of pile-up (see 'AFM-based measurements' in the *Experimental* section). They further show that pile-up leads to underestimating the projected contact area in the NI by as much as 60%⁷⁰.

One approach to exclude the contributions from the elastic deformation to the hardness measurement, while including the pile-up contribution to the projected area of the imprint, is to image the full imprint using AFM. AFM has historically been used to directly measure indentation imprints in situ, using the same probe for indenting and for imaging⁷¹, as opposed to the Oliver and Pharr method applied to nanoindenter results, which computes contact area from the indenter area function⁷². The former (AFM) approach directly parallels the classical micro-hardness test, which measures the imprint size optically, with aid of AFM made possible for nanoscale measurements. We therefore refer to hardness values obtained using the AFM image as "traditional hardness", TH . The results of this approach are presented in Fig. 5d. Comparing these results with those of

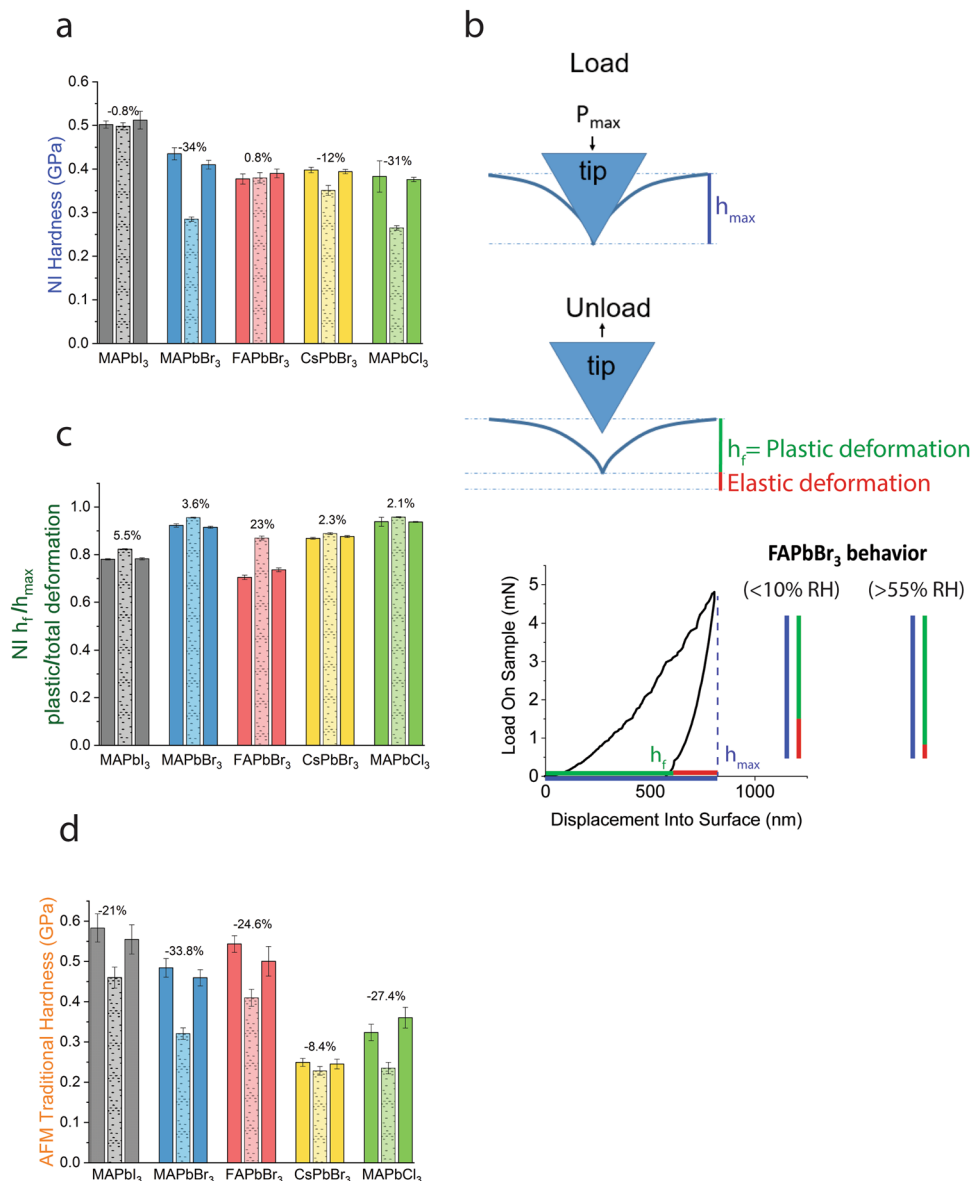


Fig. 5 Hardness measurements. **a** NI Hardness results. Solid bars represent measurements performed in the dry state; dotted bars represent measurements performed in the humid state. The percentage values here and in **c-d** represent the difference between dry and humid states for each set (see text and Fig. 2 caption). **b** Illustration of the indentation process, defining h_{max} and h_f , and explaining the trade-off between the elastic and plastic deformation in FAPbBr₃. **c** Ratio h_f/h_{max} for each of the 5 crystals under the different humidity conditions. As shown schematically in **b**, h_{max} is the depth at maximum load, and h_f is the residual depth remaining after the indenter unloads to zero load. The ratio for each crystal increases slightly in the humid state, except for FAPbBr₃, where the change is dramatic. **d** Traditional hardness (TH), calculated from the projected area of residual imprints in the AFM images for all 5 crystal types under dry and wet conditions as described in experimental section. Error bars in **a,c**, and **d** represent standard deviation in the measurements.

Fig. 5a, we see that the crystals showing a humidity effect by NI show similar response to humidity in the TH data. Two of the crystals, MAPbI₃ and FAPbBr₃, did not show a significant change in the NI hardness with humidity, but they do show a significant, reversible TH decrease at higher humidity.

We now consider, as was done for E , the influence of crystal structure on the measured hardness. The change of TH between dry and humid states for the series of anions and cations is plotted in Supplementary Fig. 8. This analysis will involve some speculation, because, whereas E is a fundamental materials property, H is not, and its value is determined by several different underlying physical contributions. We see that for both dry and humid conditions, for MAPbX₃ TH varies directly with the Pb-X

bond-length (Supplementary Figure 8). However, there is no clear trend in the change with humidity.

In the A-site cation series, the TH increases with the degree of H-bonding (with H₂O) in the order Cs < MA < FA (following the number of hydrogens available for H-bonding). However, the influence of humidity on TH is greater for MA than for FA. This is seen by comparing not absolute values of TH, but the change in value with humidity. Other considerations could be relevant here, including the stronger acidity of the amine of MA, greater stability of MA than FA, and the fact that there is more space inside the PbX framework to be filled with water molecules for MA than for FA (see above). We can thus surmise that the TH of both MAPbBr₃ and FAPbBr₃ is strongly affected by the humidity

of the environment. For a large swath of biomaterials, dehydration leads to increase of both elastic modulus and hardness, the latter indicating that water serves as a plasticizer in these materials, i.e., makes them softer, a phenomenon which seems also to occur here⁷³. The reasons for this are not fully understood, however, the tendency of organic matter to swell is likely an underlying cause in the biomaterials, a process which is akin to filling the Pb-X framework in HaPs. Although the variation in hardness in this work follows this “humidity softening” trend, the modulus varies in the opposite fashion.

The correlation between contact hardness H and indentation modulus E is well known in nano-mechanics^{67,73}. Such correlations are observed for many different material classes as expressed in Ashby plots (see, for instance ref. ⁷⁴). The unusual aspect of the correlation observed here is that it is an inverse one, not only between E and H , but also for their respective changes with humidity for several of the crystals studied (cf. Supplementary Table 1), whereas for most types of (non-HaP) materials studied this correlation is positive. We therefore propose that the inverse correlation here is due to the unique effect of water on E as discussed above. The results for MAPbI₃ need to be considered in light of the apparently higher sensitivity of this specific HaP to humidity than others, presumably due to the extreme sensitivity of this material to environmental and preparation conditions. This property was recently reported in a review, in which it was also suggested that this may result in a difference between surface and bulk properties⁷⁵. That hypothesis is confirmed here: many of the crystals prepared for the present study were seen to present crystalline faces of poor quality as revealed by AFM scans and therefore could not be used. Presumably the outer surface is most susceptible to growth-related non-idealities.

CsPbBr₃ exhibits a much smaller change in elastic modulus (Figs 2, 4) and hardness (Supplementary Table 1) with humidity than the other HaPs. This result is consistent with the importance of the strength of hydrogen bonding with the A-cation and accompanying effect of humidity on mechanical properties. It also fits with reports that the optoelectronic characteristics of Cs-based HaPs are less influenced by humidity than those of the hybrid organic-inorganic HaPs⁷⁶.

Full treatment of the humidity influence of mechanical properties on HaPs should include some considerations not discussed above. The plasticity index⁶⁶, defined as the ratio between H and E , is an important parameter that reflects the plasticity threshold of the material. Materials with large H and low E efficiently dissipate energy under load, thus increasing the plasticity threshold⁶⁷. In many materials this is a more relevant indicator of damage resistance than hardness, and, thus, critical for understanding the durability of these materials. As seen in Supplementary Table 1 the highest plasticity index values, but lowest variation with humidity were measured for MAPbI₃, while MAPbCl₃ and MAPbBr₃ have the smallest values of plasticity index but the largest change with humidity.

This study considered a series of halides, and a series of A-site cations. The B-site cation was not varied and hence we cannot directly comment on its importance in the comparisons of H-bonding effects. While H-bonding can also occur within the B-X sublattice, and the role of water interaction with the B cation in perovskite crystal formation has been heavily studied, B cation - H-bond interaction is much less implicated in the performance and mechanics of the crystal. This is largely because the B-X bond is the strongest in the crystal and less likely to form strong interactions with water^{16,22}.

Another consideration is the different effect of humidity on different crystallographic planes. This may be relevant in MAPbI₃ due to its tetragonal crystal structure at room temperature, rather than the higher temperature cubic one. MAPbCl₃, MAPbBr₃ and

FAPbBr₃ are cubic at room temperature, and, while CsPbBr₃ is orthorhombic, it is less affected by humidity due to the lower affinity toward water of Cs relative to MA and FA ions^{63,64}. Finally, significant time-dependent effects (viscoelasticity) have been reported for HaPs and this can certainly influence the measured values as reported here and elsewhere⁷⁷. Nonetheless, by performing all comparative measurements on the different crystals under identical conditions and time scales, we ensure that our results are representative and significant. This work can also be compared to almost all perovskite mechanical data found in the literature, which consider only the storage modulus.

Conclusion

While exposing MAPbCl₃, MAPbI₃, MAPbBr₃, and FAPbBr₃ to medium (55–60% RH) humidity does not degrade the materials, their elastic modulus increases by up to 10%, compared to dry conditions, an effect that is reversible. The mechanical results are consistent with independent measurements (Raman, PL, MS, x-ray) for which water is either below the detection limit, or present in small amounts and removed upon drying. The predominant response of most materials to humidity exposure is a decrease in elastic modulus (E), and we were able to correlate the unusual increase of E with intrinsic structural properties, which differ between bulk and surface. We propose that the humidity effect on E at the surface depends primarily on the interactions of the (surface-exposed) cations and anions with H₂O, as expressed by their polarity/polarizability, while the E effect in the bulk depends on the bond length and on the H-bonding options for H₂O in the material. The most significant rise in E was seen in MAPbI₃ at the surface and for FAPbBr₃ in the bulk, the latter being ascribed to H₂O diffusion during the exposure time. The mechanical properties of CsPbBr₃, in contrast to those of the other crystals studied, are not significantly dependent on the humidity, illustrating further the importance of H-bonding.

The effect of humidity on the hardness is opposite to that for the elastic modulus, with values decreasing by up to ~30% at higher humidity. While such hardness trend with humidity is common for diverse classes of other materials and is related to the plasticizing effect of water, those other materials show a direct correlation between modulus and hardness. The inverse trend seen here can be related to the unique properties of this material class as follows: Whereas modulus can be directly related to a fundamental material property, i.e., bond stiffness, hardness is a more complex property. We ascribe the hardness-humidity response to two effects, viz.

- accumulation of water within the free space of the perovskite structural framework and
- H-bond formation with suitable lattice atoms.

Because these are both common consequences of material hydration, we conclude that the unique nano-polar domains⁷⁸ and structural dynamics, namely strong dynamic disorder with high average crystalline order, of the HaPs lead to the anomalous trends in modulus^{79,80}.

While the traditional hardness, TH , values as such correlate with Pb-X bond lengths, there is no clear relation in terms of the effect of humidity on the TH (Supplementary Figure 8 and Supplementary Table 1); in fact, the strongest effect of humidity is on MAPbBr₃ and the weakest one on CsPbBr₃, which we relate to the H-bond formation ability as well as to the volume effects, discussed above.

The differences that we find in mechanical response between near-surface and bulk should be considered when using HaP crystals as radiation detectors, where the bulk dominates the response, in contrast to applications for PV and LED, where films

of small-grained (smallest dimensions ~ 400 and 50 nm, respectively) crystallites are used, into which H₂O can readily diffuse within an hour or less.

Methods

Synthesis of single crystals. Single crystals (Fig. 1) were prepared using several known crystallization methods as no single method is currently capable of synthesizing crystals of all the five compositions used here. Still, wherever possible, similar methods of crystallization were used, to minimize variations in humidity-dependent behavior on preparation technique. The methods used were:

- Inverse Temperature Crystallization (ITC)⁸¹ for MAPbI₃ and FAPbBr₃
- Anti-solvent Vapor Crystallization (AVC) for CsPbBr₃⁸² and MAPbBr₃,
- Hydrochloric Catalysis synthesis⁸³ (HC) for MAPbCl₃.

While MAPbBr₃ and CsPbBr₃ single crystals could be grown by AVC around room temperature over the time span of a few days, this was not possible for FAPbBr₃ crystals. The latter were grown by ITC, wherein the precursor solution is heated from 50 to 80 °C over a period of 5 h. A temperature ramp rate, higher than for other crystal syntheses, where relevant, was used for AVC of FAPbBr₃, as prolonged exposure to high temperatures would initiate decomposition of the DMF solvent, diminishing control over the solubility levels. After crystallization, crystals were patted dry, then placed in a vacuum oven at 35 °C for 6 h and subsequently stored under N₂ atmosphere of ~10% Relative Humidity (RH) between 3 and 10 days until measurement. Additionally, crystals were moved to a low vacuum desiccator a week prior to mechanical measurements to remove any remaining residual solvents from the primary drying phase.

Nano-indentation. High-quality crystal surfaces with well-developed smooth faces were selected using an optical microscope (Olympus AX70). Crystals were then glued to the sample stub with epoxy so that the <100> face presented orthogonally to the indenter axis, except for CsPbBr₃ for which the (101) plane was selected. Each measurement was performed on a pristine and defect-free area of the crystal, based on optical microscopy. Similar precaution was made in choosing areas for AFM measurements (below). Hardness and elastic modulus were measured using a KLA-Tencor XP Nano-indenter. The entire gantry was enclosed by a polyethylene bag in which humidity was controlled. Low humidity (≤10% RH) was achieved by a combination of two 250 g bags of “water glass” (Yamtex Sourcing) humidity absorbent sachets (SiO₂ beads), and dry nitrogen flow. The latter was stopped during measurement to avoid drift and noise. High humidity (60 % RH) was restored by activating a standard home humidifier near the nano-indenter. Humidity levels were continuously monitored by a Lutron HT-3015 humidity meter placed inside the enclosure near the sample. A Berkovich diamond indenter tip was loaded under displacement control to a depth of ~800 nm into the surface at a strain rate of 0.05 s⁻¹. The measurement was done in the “Continuous Stiffness Measurement” mode⁸⁴, yielding modulus and hardness continuously, as a function of loading. The data were analyzed using standard Oliver and Pharr analysis⁴⁹ presuming a constant Poisson ratio of 0.3 and averaged over 300–800 nm depths to avoid any surface artifacts. The Oliver and Pharr analysis calculates the tip area function from a calibration measurement on a standard sample of fused silica. Two crystals of each type were checked. For each crystal, three humidity conditions were measured in succession: low humidity (<10% RH), high humidity (55–60% RH), and finally low humidity again. After achieving the desired humidity, the crystals were equilibrated with the chosen environment for 30 min before starting the indentation experiment. At each humidity setting, 5–10 indentations were performed at different locations on the chosen face for each sample. No significant difference between the first and last of these indentations was observed, indicating that the 30 min equilibration was sufficient to reach a stable mechanical response to humidity condition. This was also the case for the AFM measurements described below. The spacing between each indentation was at least 18 times the indentation depth of 0.8 μm to avoid interference between the measurements. This spacing is generally sufficient to avoid interference due to any material changes such as dislocations from neighboring indentations^{71,85}. We further verified that there was no significant difference between the first indentation, and subsequent ones in the set. Supplementary Figure 6 shows sets of indentations made under dry and humid conditions on MAPbI₃ and on FAPbBr₃. All measurements were made at room temperature which varied between 21 and 24 °C.

AFM-based measurements. Sample treatment for AFM prior to measurements was the same as that for nano-indentation. Two types of measurements were performed using the AFM, viz., traditional hardness (*TH*; including topography) and contact resonance (CR). Both *TH* and CR measurements (*vide infra*) were conducted using a Multimode AFM with Nanoscope V electronics (Bruker, USA). The *TH*-AFM measurements used a 222 N/m cantilever probe with a diamond shard tip, glued to it (Microstar-Tech) to indent the crystal surface. The same AFM probe was used to image the surface and locate a smooth area (typically ranging from 1–2 nm but never more than ~5 nm in RMS roughness over a 4 × 4 μm² field of view) for the indentation experiment. The sensitivity of the probe (nm/V) was calibrated by pressing on a sapphire surface. Indentations were performed up to a load of 81 μN which resulted in depths ranging from 100–200 nm, depending on the crystal and humidity. The indentation path compensated for the approximately

12° angle between the cantilever and surface by adding a component of x motion (along the cantilever long axis) to the z approach. This uses a feature termed “x-rotation” in the Bruker ramping software. Several angles above and below 12 degrees were tested to obtain the most symmetric form of indentation (see Supplementary Fig. 9). At each humidity level, the crystal was equilibrated for 30 minutes prior to measurement. Then 8 indentations were made with a 2.2 μm separation between neighboring indentations. After indenting, the surface was imaged to map the topography of the indentation and the area surrounding the indentations, as the resulting pile-up next to the indentation is critical for computing hardness values accurately.

The elastic modulus was determined using the Bruker software by the contact resonance (CR-AFM) method, the analysis of which combines Euler-Bernoulli beam dynamics with contact mechanics principles^{86–89}. In this analysis, we did not consider viscoelastic effects. To a good approximation the associated loss modulus can be treated independently from the storage modulus. The latter depends on the contact frequency, and the former on both the width of the contact resonance peak and its frequency⁸⁸. The Bruker fast force volume contact resonance software package was used to supply the measurement conditions and analyze the resultant data. In this method a frequency sweep at fixed amplitude is applied to the cantilever support or the sample holder and amplitude vs. frequency sweeps over a fixed frequency range are collected for a grid of sample locations. We further modified the system by connecting the signal to a 2.4 MHz ultrasonic Mist Maker fogger piezoelectric disk which mechanically excited the sample from below. The sample was coupled to the disk with a drop of honey to provide good acoustic coupling and allow for easy sample exchange⁹⁰. The contact area of the back of the sample with the transducer was 10 orders of magnitude larger than the tip-surface contact area; therefore, no influence of the back contact is expected. The probe used was tungsten-carbide coated HA_HR/W2C (ScanSens, Germany). The out-of-plane vibrations from the sample surface were transmitted to the cantilever via the tip which is pressed into the surface with a pre-set force. Under these conditions, the resulting contact frequency is directly dependent on the contact stiffness (*k*). By making a similar measurement on a standard sample, the effective tip radius is determined which together with the measured contact stiffness can be used to calculate the elastic modulus of the sample. These measurements were made with small indentations, on the order of a nm up to a few nm and are sensitive to the upper 20–30 nm of the surface under typical conditions.

To accurately calculate the traditional hardness, the projected surface area of the residual indentation imprints was calculated from the AFM images. The projected area of the depression for each imprint was determined using the “Analyze Imprint” function in Gwyddion software³⁶. The size of the surrounding pile-up was computed using the dimensions from the topography image, and the method described by Cabibbo et al., to calculate the contribution of the pile-up to the total projected surface area⁹¹.

To control humidity, the “Humidity plug” for the AFM was used to seal the opening of the small measurement cavity and humidity-controlled gas was flown in using a flexible tube. The home-built humidity setup combined wet and dry nitrogen in a mixing chamber and controlled relative humidity over the range 5% – 80% with +/– 1% RH accuracy. An electronic feedback-controlled a solenoid valve and allowed setting the humidity to the desired value.

Pb-X bond length calculation. We used as the Pb-X bond length half of the cubic unit cell side (which contains just one formula unit), obtaining 2.84 Å for MAPbCl₃⁹², 2.97 Å MAPbBr₃⁹³, and 3.01 Å FAPbBr₃⁹⁴. In orthorhombic CsPbBr₃ and tetragonal MAPbI₃ (all at and around room temperature), not all three unit cell axes are equal and the unit cell contains 4 formula units. The bond length was evaluated considering the volume per formula unit (volume of the unit cell 796.66 Å³ for CsPbBr₃⁹⁵ and 992.49 for MAPbI₃⁹⁶ divided by 4), taking the cubic root and finally dividing the value by 2 to obtain 2.92 Å and 3.14 Å for CsPbBr₃ and MAPbI₃ respectively.

Data availability

All relevant data are available from the authors upon reasonable request.

Received: 14 June 2022; Accepted: 30 August 2022;

Published online: 04 October 2022

References

- Chen, Q. et al. Under the spotlight: The organic-inorganic hybrid halide perovskite for optoelectronic applications. *Nano Today* **10**, 355–396 (2015).
- Kovalenko, M. V., Protesescu, L. & Bodnarchuk, M. I. Properties and potential optoelectronic applications of lead halide perovskite nanocrystals. *Science* **358**, 745–750 (2017).
- Yang, M. et al. Facile fabrication of large-grain CH₃NH₃PbI₃-xBrx films for high-efficiency solar cells via CH₃NH₃Br-selective Ostwald ripening. *Nat. Commun.* **7**, 12305 (2016).

4. Wang, Y., Zhang, T., Xu, F., Li, Y., Zhao, Y. A Facile Low Temperature Fabrication of High Performance CsPbI₂Br All-Inorganic Perovskite Solar Cells. *Solar RRL* **2**, 1700180 (2018).
5. Stranks, S. D. et al. Electron-hole diffusion lengths exceeding 1 micrometer in an organometal trihalide perovskite absorber. *Science* **342**, 341–344 (2013).
6. Dong, Q. et al. Electron-hole diffusion lengths > 175 μm in solution-grown CH₃NH₃PbI₃ single crystals. *Science* **347**, 967–970 (2015).
7. Miyasaka, T. Perovskite photovoltaics: Rare functions of organo lead halide in solar cells and optoelectronic devices. *Chem. Lett.* **44**, 720–729 (2015).
8. Kim, H. S., Im, S. H. & Park, N. G. Organolead halide perovskite: New horizons in solar cell research. *J. Phys. Chem. C* **118**, 5615–5625 (2014).
9. Dang, Y. et al. Bulk Chiral Halide Perovskite Single Crystals for Active Circular Dichroism and Circularly Polarized Luminescence. *J. Phys. Chem. Lett.* **11**, 1689–1696 (2020).
10. Hu, X. et al. High-performance flexible broadband photodetector based on organolead halide perovskite. *Adv. Funct. Mater.* **24**, 7373–7380 (2014).
11. Service, R. F. Energy technology: Perovskite solar cells keep on surging. *Science* **344**, 458–458 (2014).
12. Snaith, H. J. Perovskites: The emergence of a new era for low-cost, high-efficiency solar cells. *J. Phys. Chem. Lett.* **4**, 3623–3630 (2013).
13. Kind, H., Yan, H., Messer, B., Law, M. & Yang, P. Nanowire ultraviolet photodetectors and optical switches. *Adv. Mater.* **14**, 158–160 (2002).
14. Leung, S. F. et al. A Self-Powered and Flexible Organometallic Halide Perovskite Photodetector with Very High Detectivity. *Adv. Mater.* **30**, 1704611 (2018).
15. Lee, M., Jo, Y., Kim, D. S. & Jun, Y. Flexible organo-metal halide perovskite solar cells on a Ti metal substrate. *J. Mater. Chem. A* **3**, 4129–4133 (2015).
16. Huang, J., Tan, S., Lund, P. D. & Zhou, H. Impact of H₂O on organic–inorganic hybrid perovskite solar cells. *Energy Environ. Sci.* **10**, 2284–2311 (2017).
17. Howard, J. M. et al. Humidity-Induced Photoluminescence Hysteresis in Variable Cs/Br Ratio Hybrid Perovskites. *J. Phys. Chem. Lett.* **9**, 3463–3469 (2018).
18. Manshor, N. A. et al. Humidity: Versus photo-stability of metal halide perovskite films in a polymer matrix. *Phys. Chem. Chemical Phys.* **18**, 21629–21639 (2016).
19. Di Girolamo, D. et al. Dual effect of humidity on cesium lead bromide: Enhancement and degradation of perovskite films. *J. Mater. Chem. A* **7**, 12292–12302 (2019).
20. Bhatt, P., Kumar, M., Chandra Kant, P., Pandey, M. K. & Tripathi, B. Optoelectronic modelling of perovskite solar cells under humid conditions and their correlation with power losses to quantify material degradation. *Org. Electron.* **39**, 258–266 (2016).
21. Cheng, S. & Zhong, H. What Happens When Halide Perovskites Meet with Water? *J. Phys. Chem. Lett.* **13**, 2281–2290 (2022).
22. Chen, B., Wang, S., Song, Y., Li, C. & Hao, F. A critical review on the moisture stability of halide perovskite films and solar cells. *Chem. Eng. J.* **430**, 132701 (2022).
23. Christians, J. A., Herrera, P. A. M. & Kamat, P. V. Transformation of the Excited State and Photovoltaic Efficiency of CH₃NH₃PbI₃ Perovskite upon Controlled Exposure to Humidified Air. *J. Am. Chem. Society* **137**, 1530–1538 (2015).
24. Yang, J., Siempelkamp, B. D., Liu, D. & Kelly, T. L. Investigation of CH₃NH₃PbI₃ Degradation Rates and Mechanisms in Controlled Humidity Environments Using in Situ Techniques. *ACS Nano* **9**, 1955–1963 (2015).
25. Leguy, A. M. A. et al. Reversible Hydration of CH₃NH₃PbI₃ in Films, Single Crystals, and Solar Cells. *Chem. Mater.* **27**, 3397–3407 (2015).
26. Kakekhani, A., Katti, R. N. & Rappe, A. M. Water in hybrid perovskites: Bulk MAPbI₃ degradation via super-hydrated state. *APL Materials* **7**, 041112 (2019).
27. Schlipf, J. et al. In Situ Monitoring the Uptake of Moisture into Hybrid Perovskite Thin Films. *J. Phys. Chem. Lett.* **9**, 2015–2021 (2018).
28. Philippe, B. et al. Chemical and Electronic Structure Characterization of Lead Halide Perovskites and Stability Behavior under Different Exposures—A Photoelectron Spectroscopy Investigation. *Chem. Mater.* **27**, 1720–1731 (2015).
29. Noh, J. H., Im, S. H., Heo, J. H., Mandal, T. N. & Seok, S. I. Chemical Management for Colorful, Efficient, and Stable Inorganic–Organic Hybrid Nanostructured Solar Cells. *Nano Lett.* **13**, 1764–1769 (2013).
30. Li, Q. et al. Compositional effect on water adsorption on metal halide perovskites. *Appl. Surf. Sci.* **538**, 148058 (2021).
31. Koocher, N. Z., Saldana-Greco, D., Wang, F., Liu, S. & Rappe, A. M. Polarization Dependence of Water Adsorption to CH₃NH₃PbI₃ (001) Surfaces. *J. Phys. Chem. Lett.* **6**, 4371–4378 (2015).
32. Zhu, Z. et al. Interaction of Organic Cation with Water Molecule in Perovskite MAPbI₃: From Dynamic Orientational Disorder to Hydrogen Bonding. *Chem. Mater.* **28**, 7385–7393 (2016).
33. Liao, W.-C., Liu, B. H. & Leu, C.-C. Nanoscale mapping of humid degradation-induced local mechanical property variation in CH₃NH₃PbI₃ polycrystalline film by scanning probe microscopy. *Appl. Surf. Sci.* **507**, 145078 (2020).
34. Frost, J. M. et al. Atomistic Origins of High-Performance in Hybrid Halide Perovskite Solar Cells. *Nano Lett.* **14**, 2584–2590 (2014).
35. Zhang, L. & Sit, P. H. L. Ab Initio Study of Interaction of Water, Hydroxyl Radicals, and Hydroxide Ions with CH₃NH₃PbI₃ and CH₃NH₃PbBr₃ Surfaces. *J. Phys. Chem. C* **119**, 22370–22378 (2015).
36. Mosconi, E., Azpiroz, J. M. & De Angelis, F. Ab Initio Molecular Dynamics Simulations of Methylammonium Lead Iodide Perovskite Degradation by Water. *Chem. Mater.* **27**, 4885–4892 (2015).
37. Tong, C.-J. et al. Uncovering the Veil of the Degradation in Perovskite CH₃NH₃PbI₃ upon Humidity Exposure: A First-Principles Study. *J. Phys. Chem. Lett.* **6**, 3289–3295 (2015).
38. Mamun, A. A., Mohammed, Y., Ava, T. T., Namkoong, G. & Elmustafa, A. A. Influence of air degradation on morphology, crystal size and mechanical hardness of perovskite film. *Mater. Lett.* **229**, 167–170 (2018).
39. Chudoba, T. Measurement of Hardness and Young's Modulus by Nanoindentation. In *Nanostructured Coatings*, (eds. Cavaleiro, A., De Hosson, J. T. M.) 216–260 (Springer New York: New York, NY, 2006).
40. Spina, M. et al. Mechanical signatures of degradation of the photovoltaic perovskite CH₃NH₃PbI₃ upon water vapor exposure. *Appl. Phys. Lett.* **110**, 121903 (2017).
41. Aristidou, N. et al. The Role of Oxygen in the Degradation of Methylammonium Lead Trihalide Perovskite Photoactive Layers. *Angew. Chem.* **127**, 8326–8330 (2015).
42. Kim, J., Lee, S. H., Chung, C. H. & Hong, K. H. Systematic analysis of the unique band gap modulation of mixed halide perovskites. *Phys. Chem. Chem. Phys.* **18**, 4423–4428 (2016).
43. Rakita, Y., Cohen, S. R., Kedem, N. K., Hodes, G. & Cahen, D. Mechanical properties of APbX₃ (A = Cs or CH₃NH₃; X = I or Br) perovskite single crystals. *MRS Commun.* **5**, 623–629 (2015).
44. Sun, S., Fang, Y., Kieslich, G., White, T. J. & Cheetham, A. K. Mechanical properties of organic–inorganic halide perovskites, CH₃NH₃PbX₃ (X = I, Br and Cl), by nanoindentation. *J. Mater. Chem. A* **3**, 18450–18455 (2015).
45. Wang, B. et al. Room-temperature water-vapor annealing for high-performance planar perovskite solar cells. *J. Mater. Chem. A* **4**, 17267–17273 (2016).
46. Petrus, M. L. et al. The Influence of Water Vapor on the Stability and Processing of Hybrid Perovskite Solar Cells Made from Non-Stoichiometric Precursor Mixtures. *ChemSusChem* **9**, 2699–2707 (2016).
47. Zhou, W. et al. Reversible Healing Effect of Water Molecules on Fully Crystallized Metal–Halide Perovskite Film. *J. Phys. Chem. C* **120**, 4759–4765 (2016).
48. Ceratti, D. R. et al. Self-Healing and Light-Soaking in MAPbI₃: The Effect of H₂O. *Adv. Mater.* **34**, 2110239 (2022).
49. Oliver, W. C. & Pharr, G. M. Measurement of hardness and elastic modulus by instrumented indentation: Advances in understanding and refinements to methodology. *J. Mater. Res.* **19**, 3–20 (2004).
50. Cohen, S. R. & Kalfon-Cohen, E. Dynamic nanoindentation by instrumented nanoindentation and force microscopy: a comparative review. *Beilstein J. Nanotechnol.* **4**, 815–833 (2013).
51. Ji, L.-J., Sun, S.-J., Qin, Y., Li, K. & Li, W. Mechanical properties of hybrid organic–inorganic perovskites. *Coord. Chem. Rev.* **391**, 15–29 (2019).
52. ISO/FDIS. *Metallic materials-Instrumented indentation test for hardness and materials parameters -Part1:Test method.* (Geneve, Switzerland, 2015).
53. Ma, L. et al. A- or X-site mixture on mechanical properties of APbX₃ perovskite single crystals. *APL Materials* **9**, 041112 (2021).
54. Zhang, Y., Kim, S.-G., Lee, D., Shin, H. & Park, N.-G. Bifacial stamping for high efficiency perovskite solar cells. *Energy Environ. Sci.* **12**, 308–321 (2019).
55. Cabibbo, M. et al. An international round-robin calibration protocol for nanoindentation measurements. *Micron* **43**, 215–222 (2012).
56. Ceratti, D. R. et al. Eppur si Muove: Proton Diffusion in Halide Perovskite Single Crystals. *Adv. Mater.* **32**, 2002467 (2020).
57. Buffeteau, T., Hirsch, L. & Bassani, D. M. Comment on “Eppur si Muove: Proton Diffusion in Halide Perovskite Single Crystals”: Eppur Non si Muove: A Critical Evaluation of Proton Diffusion in Halide Perovskite Single Crystals. *Adv. Mater.* **33**, 2007715 (2021).
58. Ceratti, D. R., Zohar, A., Hodes, G. & Cahen, D. Response to Comment on “Eppur si Muove: Proton Diffusion in Halide Perovskite Single Crystals”: Measure What is Measurable, and Make Measurable What is Not So: Discrepancies between Proton Diffusion in Halide Perovskite Single Crystals and Thin Films. *Adv. Mater.* **33**, 2102822 (2021).
59. Jasti, N. P. et al. The Saga of Water and Halide Perovskites: Evidence of Water in Methylammonium Lead Tri-Iodide. *Adv. Funct. Mater.* **32**, 2204283 (2022).

60. Yu, J., Wang, M. & Lin, S. Probing the Soft and Nanoductile Mechanical Nature of Single and Polycrystalline Organic-Inorganic Hybrid Perovskites for Flexible Functional Devices. *ACS Nano* **10**, 11044–11057 (2016).
61. Kieslich, G., Sun, S. & Cheetham, A. K. An extended Tolerance Factor approach for organic-inorganic perovskites. *Chemical Science* **6**, 3430–3433 (2015).
62. Oranskaia, A., Yin, J., Bakr, O. M., Brédas, J.-L. & Mohammed, O. F. Halogen Migration in Hybrid Perovskites: The Organic Cation Matters. *Journal of Physical Chemistry Letters* **9**, 5474–5480 (2018).
63. Mähler, J. & Persson, I. A Study of the Hydration of the Alkali Metal Ions in Aqueous Solution. *Inorganic Chem.* **51**, 425–438 (2012).
64. Greenwood, N. N. & Earnshaw, A. *Chemistry of the Elements*. Elsevier: 2012.
65. Sun, S. et al. Factors Influencing the Mechanical Properties of Formamidinium Lead Halides and Related Hybrid Perovskites. *ChemSusChem* **10**, 3740–3745 (2017).
66. Cheng, Y.-T. & Cheng, C.-M. Relationships between hardness, elastic modulus, and the work of indentation. *Appl. Phys. Lett.* **73**, 614–616 (1998).
67. Rosenhek-Goldian, I. & Cohen, S. R. Nanomechanics of Biomaterials – from Cells to Shells. *Isr. J. Chem.* **60**, 1171–1184 (2020).
68. Chen, J. & Bull, S. J. Relation between the ratio of elastic work to the total work of indentation and the ratio of hardness to Young's modulus for a perfect conical tip. *J. Mater. Res.* **24**, 590–598 (2009).
69. Giannakopoulos, A. E. & Suresh, S. Determination of elastoplastic properties by instrumented sharp indentation. *Scripta Mater* **40**, 1191–1198 (1999).
70. Bolshakov, A. & Pharr, G. M. Influences of pileup on the measurement of mechanical properties by load and depth sensing indentation techniques. *J. Mater. Res.* **13**, 1049–1058 (1998).
71. Cohen, S. R. et al. AFM Investigation of Mechanical Properties of Dentin. *Isr. J. Chem.* **48**, 65–72 (2008).
72. Herrmann, K. et al. Progress in determination of the area function of indenters used for nanoindentation. *Thin Solid Films* **377–378**, 394–400 (2000).
73. Labonte, D., Lenz, A.-K. & Oyen, M. L. On the relationship between indentation hardness and modulus, and the damage resistance of biological materials. *Acta Biomater* **57**, 373–383 (2017).
74. Tan, J. C. & Cheetham, A. K. Mechanical properties of hybrid inorganic-organic framework materials: establishing fundamental structure-property relationships. *Chem. Soc. Rev.* **40**, 1059–1080 (2011).
75. Tu, Q., Kim, D., Shykh, M. & Kanatzidis, M. G. Mechanics-coupled stability of metal-halide perovskites. *Matter* **4**, 2765–2809 (2021).
76. Duan, Y. et al. Highly efficient and stable inorganic CsPbBr₃ perovskite solar cells via vacuum co-evaporation. *Appl. Surf. Sci.* **562**, 150153 (2021).
77. Reyes-Martinez, M. A. et al. Time-Dependent Mechanical Response of APbX₃ (A = Cs, CH₃NH₃; X = I, Br) Single Crystals. *Adv. Mater.* **29**, 1606556 (2017).
78. Schilcher, M. J. et al. The Significance of Polarons and Dynamic Disorder in Halide Perovskites. *ACS Energy Lett.* **6**, 2162–2173 (2021).
79. Mayers, M. Z., Tan, L. Z., Egger, D. A., Rappe, A. M. & Reichman, D. R. How Lattice and Charge Fluctuations Control Carrier Dynamics in Halide Perovskites. *Nano Lett* **18**, 8041–8046 (2018).
80. Kumar, S., Hodes, G. & Cahen, D. Defects in halide perovskites: The lattice as a boojum? *MRS Bull* **45**, 478–484 (2020).
81. Saidaminov, M. I. et al. High-quality bulk hybrid perovskite single crystals within minutes by inverse temperature crystallization. *Nat. Commun.* **6**, 7586 (2015).
82. Rakita, Y. et al. Low-Temperature Solution-Grown CsPbBr₃ Single Crystals and Their Characterization. *Cryst. Growth Des.* **16**, 5717–5725 (2016).
83. Shamsi, J. et al. N-Methylformamide as a Source of Methylammonium Ions in the Synthesis of Lead Halide Perovskite Nanocrystals and Bulk Crystals. *ACS Energy Lett.* **1**, 1042–1048 (2016).
84. Li, X. & Bhushan, B. A review of nanoindentation continuous stiffness measurement technique and its applications. *Mater. Charact.* **48**, 11–36 (2002).
85. Ziskind, D., Hasday, M., Cohen, S. R. & Wagner, H. D. Young's modulus of peritubular and intertubular human dentin by nano-indentation tests. *J. Struct. Biol.* **174**, 23–30 (2011).
86. Rabe, U. et al. Imaging and measurement of local mechanical material properties by atomic force acoustic microscopy. *Surf. Interface Anal.* **33**, 65–70 (2002).
87. Rabe, U. & Arnold, W. Acoustic microscopy by atomic force microscopy. *Appl. Phys. Lett.* **64**, 1493–1495 (1994).
88. Killgore, J. P. & DelRio, F. W. Contact Resonance Force Microscopy for Viscoelastic Property Measurements: From Fundamentals to State-of-the-Art Applications. *Macromolecules* **51**, 6977–6996 (2018).
89. Yuya, P. A., Hurley, D. C. & Turner, J. A. Contact-resonance atomic force microscopy for viscoelasticity. *J. Appl. Phys.* **104**, 074916 (2008).
90. Netshidavhini, N. & Mabuza, R. B. Effects of Various Couplants on Carbon Steel and Aluminium Materials Using Ultrasonic Testing In *18th World Conference on Nondestructive Testing*, Durban, South Africa (2012).
91. Cabibbo, M., Ciccarelli, D. & Spigarelli, S. Nanoindentation Hardness measurement in piling up SiO₂ coating. *Phys. Procedia* **40**, 100–112 (2013).
92. Caputo, M. et al. Electronic structure of MAPbI₃ and MAPbCl₃: importance of band alignment. *Sci. Rep.* **9**, 15159 (2019).
93. Zhao, P. et al. Large-Size CH₃NH₃PbBr₃ Single Crystal: Growth and In Situ Characterization of the Photophysics Properties. *J. Phys. Chem. Lett.* **6**, 2622–2628 (2015).
94. Govinda, S. et al. Critical Comparison of FAPbX₃ and MAPbX₃ (X = Br and Cl): How Do They Differ? *J. Phys. Chem. C* **122**, 13758–13766 (2018).
95. Rodová, M., Brožek, J., Knížek, K. & Nitsch, K. Phase transitions in ternary caesium lead bromide. *J. Therm. Anal. Calorim* **71**, 667–673 (2003).
96. López, C. A., Alvarez-Galván, M. C., Martínez-Huerta, M. V., Fauth, F. & Alonso, J. A. Crystal structure features of CH₃NH₃PbI₃-xBr_x hybrid perovskites prepared by ball milling: a route to more stable materials. *CrystEngComm* **22**, 767–775 (2020).

Acknowledgements

We thank Guy Reuveni and Dr. Omer Yaffe (Weizmann Inst.) for the Raman spectroscopy measurements, Dr. Gili Cohen-Taguri (BIU) for her expert assistance with the humidity-dependent XRD measurements and Prof. Ilya Grinberg (BIU) and Ms. Anat Itzhak (BIU) for fruitful discussions and ideas. DRC thanks the European Union's Horizon 2020 research and innovation program under the Marie Skłodowska-Curie grant agreement No. 893194. NPJ acknowledges funding from the European Union's Horizon 2020 MSCA Innovative Training Network MAESTRO under grant agreement no. 764787 at BIU. At BIU this work was further supported by the Israel Ministry of Energy as part of the SolarERAnet PERDRY consortium. At the Weizmann Institute the work was supported by the Yotam project, the Minerva Centre for Self-Repairing Systems for Energy & Sustainability, and the CNRS-Weizmann program.

Author contributions

S.R.C. and D.C. conceived the project. D. C., S.R.C. and I.R.G. wrote the manuscript. I.R.G. and S.R.C. designed the AFM and NI experiments. I.R.G. and I.B. performed the AFM and NI experiments and analyzed the data. N.P.J. and I.B. synthesized the crystals. D.R.C. performed the bond length calculations. SK performed and interpreted the PL measurements. All authors contributed to the discussions on, and writing of the final versions of the manuscript and SI.

Competing interests

The authors declare no competing interests.

Additional information

Supplementary information The online version contains supplementary material available at <https://doi.org/10.1038/s43246-022-00287-7>.

Correspondence and requests for materials should be addressed to David Cahen or Sidney R. Cohen.

Peer review information *Communications Materials* thanks the anonymous reviewers for their contribution to the peer review of this work. Primary Handling Editor: John Plummer. Peer reviewer reports are available.

Reprints and permission information is available at <http://www.nature.com/reprints>

Publisher's note Springer Nature remains neutral with regard to jurisdictional claims in published maps and institutional affiliations.



Open Access This article is licensed under a Creative Commons Attribution 4.0 International License, which permits use, sharing, adaptation, distribution and reproduction in any medium or format, as long as you give appropriate credit to the original author(s) and the source, provide a link to the Creative Commons license, and indicate if changes were made. The images or other third party material in this article are included in the article's Creative Commons license, unless indicated otherwise in a credit line to the material. If material is not included in the article's Creative Commons license and your intended use is not permitted by statutory regulation or exceeds the permitted use, you will need to obtain permission directly from the copyright holder. To view a copy of this license, visit <http://creativecommons.org/licenses/by/4.0/>.

© The Author(s) 2022